AIAA JOURNAL
Vol. 53, No. 8, August 2015

Discrete-Roughness-Element-Enhanced Swept-Wing Natural Laminar Flow at High Reynolds Numbers

Mujeeb Malik*
NASA Langley Research Center, Hampton, Virginia 23681
Wei Liao†
National Institute of Aerospace, Hampton, Virginia 23666
and
Fei Li‡ and Meelan Choudhari§
NASA Langley Research Center, Hampton, Virginia 23681

DOI: 10.2514/1.J053637

Nonlinear parabolized stability equations and secondary-instability analyses are used to provide a computational assessment of the potential use of the discrete-roughness-element technology for extending swept-wing natural laminar flow at chord Reynolds numbers relevant to transport aircraft. Computations performed for the boundary layer on a natural-laminar-flow airfoil with a leading-edge sweep angle of 34.6 deg, freestream Mach number of 0.75, and chord Reynolds numbers of 17×10^6, 24×10^6, and 30×10^6 suggest that discrete roughness elements could delay laminar–turbulent transition by about 20% when transition is caused by stationary crossflow disturbances. Computations show that the introduction of small-wavelength stationary crossflow disturbances (i.e., discrete roughness element) also suppresses the growth of most amplified traveling crossflow disturbances.

Nomenclature

A_{ini}	=	initial disturbance amplitude
C	=	wing/airfoil chord length
C_L	=	lift coefficient
C_p	=	pressure coefficient
f	=	disturbance frequency
H	=	flight altitude
M	=	freestream Mach number
m	=	time Fourier mode number
N	=	N factor
n	=	spanwise Fourier mode number
R_{cf}	=	crossflow Reynolds number
Re_c	=	Reynolds number based on wing chord
Tu	=	turbulence level in the freestream
U_c	=	velocity component in the crossflow direction
U_s	=	velocity in the inviscid streamline direction
$W_{\max}$	=	maximum crossflow velocity in a crossflow-velocity profile
X	=	chordwise coordinate (in a direction normal to the leading edge)
x	=	chordwise surface coordinate (in a direction normal to the leading edge)
x_0	=	chord surface location where perturbation is initialized
Y	=	distance from center of the aircraft fuselage
y	=	wall normal coordinate
Z	=	spanwise coordinate in traveling frame of reference
z	=	spanwise coordinate
α_{mn}	=	chordwise wave number of Fourier mode (m, n)
β	=	fundamental spanwise wave number
$\delta_{0.1}$	=	distance from wall where the crossflow velocity reduces to 10% of $W_{\max}$
ν_e	=	kinematic viscosity at boundary-layer edge
ξ	=	dummy variable for chordwise integration
ϕ	=	any perturbation field variable
$\hat{\phi}$	=	Fourier transform of ϕ

Presented as Paper 2013-0412 at the 51st AIAA Aerospace Sciences Meeting, Grapewine, TX, 7–10 January 2013; received 23 June 2014; revision received 14 October 2014; accepted for publication 16 October 2014; published online 12 March 2015.

*Senior Aerodynamicist, Computational AeroSciences Branch, MS 128; Mujeeb.R.Malik@nasa.gov. Fellow AIAA.
†Research Scientist; Wei.Liao@nasa.gov. Senior Member AIAA.
‡Aerospace Technologist, Computational AeroSciences Branch, MS 128; Fei.Li@nasa.gov.
§Aerospace Technologist, Computational AeroSciences Branch, MS 128; Meelan.M.Choudhari@nasa.gov. Associate Fellow AIAA.

I. Introduction

SKIN friction constitutes about 50% of the drag budget of a business jet or a long-haul transport aircraft [1,2]. Therefore, reduction in skin friction has the potential of yielding substantial savings in fuel burn. According to a system study [3], fuel burn savings in access of 9% are achievable for transport aircraft. Because laminar skin friction is much less than the turbulent value, the subject of maintaining laminar flow for high-Reynolds-number flows (i.e., delay of boundary-layer transition) has been of interest for well over half a century; see [4–8] for reviews of the subject.

In the low-amplitude freestream disturbance environment typical of subsonic flight applications, transition in two-dimensional boundary layers is caused by Tollmien–Schlichting (TS) instability, which can be controlled by favorable pressure gradients, wall suction, and wall heat transfer (cooling in air, heating in water). Transition in three-dimensional (3-D) swept-wing boundary layers can also be caused by crossflow instability, which often manifests itself in the form of stationary corotating streamwise vortices that originate at minute roughness sites [9,10]. These vortices break down via a high-frequency secondary-instability mechanism [11–15]. Crossflow instability can be controlled by using wall suction, and experimental campaigns for demonstrating laminar-flow control (LFC) using suction have been conducted in subsonic [16–18] as well as in supersonic [19] flight.

Crossflow-instability results due to an inflection point in the crossflow-velocity component (i.e., the component in the direction normal to the inviscid streamlines) and minimizing this velocity component would weaken the instability and yield extended runs of laminar flow. For a given leading-edge sweep angle and unit Reynolds number, the only way to reduce the crossflow-velocity component is to minimize the chordwise pressure gradient, but that would result in amplification of the TS instability, which is enhanced under less favorable pressure gradients. Thus, swept-wing natural-laminar-flow (NLF) design is based upon striking a delicate balance

by tailoring the pressure distribution such that the crossflow instability is reduced sufficiently while keeping TS growth at subcritical levels with respect to transition. One can only maintain this balance for a limited range of chord Reynolds numbers, and so LFC via suction must be employed if laminar flow is desired at high Reynolds numbers associated with large transport aircraft.

The wavelength of crossflow disturbances scales with the boundary-layer thickness, with small-wavelength disturbances growing first (i.e., at small distance from the wing leading edge), but decaying over relatively small distances. The longer wavelength disturbances become unstable farther downstream, but remain unstable over longer streamwise distances, and eventually break down via secondary instabilities that lead to laminar–turbulent transition. Saric et al. [20] discovered that forcing small-wavelength disturbances (i.e., the "control" mode) at relatively high amplitudes changes the boundary-layer mean flow, such that the growth of more dominant larger-wavelength disturbances (i.e., the "target" mode) is pushed downstream, thus delaying transition. This concept has been studied by using nonlinear parabolized stability equations (NPSEs) [21] and direct numerical simulations (DNSs) [22]. Both these analyses support the soundness of the fundamental concept. In practice, the control mode is introduced via discrete spanwise periodic roughness elements placed near the neutral point of the instability diagram. These control disturbances only introduce harmonics and no subharmonics, and therefore, do not directly feed into the larger-wavelength target modes. This strategy for controlling crossflow disturbances is known as discrete-roughness-element (DRE) technology, and has the potential to increase the range of applicability of NLF to higher chord Reynolds numbers. Computations based on NPSE and secondary-instability analysis have been performed for subsonic swept-wing designs at Reynolds numbers of 7.15×10^6 and 17×10^6, which showed that DRE could delay the growth of the stationary target modes and the associated secondary instabilities at these Reynolds numbers [23,24].

Saric et al. [25] reported a flight experiment using Cessna O-2 aircraft to demonstrate the DRE concept. The test article consisted of a 30 deg swept blade that was mounted vertically under one of the wings of the aircraft. The maximum transition Reynolds number obtained on the test article was about 6.4×10^6 when the leading edge was polished with a surface finish quoted as 0.3 μm rms and 2.2 μm average peak to peak. Here, the transition Reynolds number was limited by a pressure minimum (i.e., adverse pressure gradient) because of the relatively low chord Reynolds number of 8×10^6. In other words, an increased extent of the NLF could be had for a larger test article. When the leading edge was painted to yield a deteriorated surface finish (quoted as 1 μm rms, with 3.8 μm peak to peak), the transition Reynolds number dropped to about 2.4×10^6 owing to the adverse effect of surface roughness on transition; with the application of DRE, the transition Reynolds number increased to about 4.8×10^6 for the chord Reynolds number of 8×10^6. This is the highest Reynolds number at which the DRE technology has been demonstrated to delay crossflow-induced transition. Clearly, NLF could be maintained at such Reynolds numbers without the use of DRE, and there is a need to demonstrate the technology at higher chord Reynolds numbers, Mach numbers, and lift coefficients of relevance to transport aircraft.

NASA's Environmentally Responsible Aviation (ERA) Project sponsored the evaluation of DRE as an LFC technology for potential application to transport aircraft. A collaborative effort between NASA Armstrong Flight Research Center, NASA Langley Research Center, and Texas A&M University (TAMU) was initiated to design a flight experiment using NASA Armstrong Flight Research Center's Gulfstream-III (G-III, hereinafter G-3) aircraft. A wing glove was designed by TAMU, with the glove leading-edge sweep of 34.6 deg with a maximum possible chord Reynolds number approaching 30×10^6. The details of the glove design and analyses using computational fluid dynamics and stability-analysis codes have been given in [26–30].

This paper provides an assessment of the DRE applicability to high-Reynolds-number flows using NPSEs and secondary-instability analysis, extending the previous results obtained for a different airfoil design in [24]. The particular conditions used for the assessment consist of a freestream Mach number of 0.75 and Reynolds numbers of 17×10^6, 24×10^6, and 30×10^6. A small-wavelength subcritical stationary crossflow disturbance (i.e., the control mode) is introduced to study its effect on the nonlinear evolution of the longer wavelength, most amplified stationary crossflow disturbances (i.e., the target mode). Secondary-instability analyses of the target mode with and without control were performed to provide an assessment of the ability of DRE to delay laminar–turbulent transition at high Reynolds numbers. The initial amplitudes of the target and control modes were assumed, and the modal shapes were taken from the stability analysis. Thus, the impact of the actual surface roughness to initiate natural crossflow disturbances, as well as the control mode, was not simulated, as this simulation is not trivial and was considered outside the scope of the present study.

Traveling disturbances of the crossflow type are also amplified by the boundary layer, and, in fact, these disturbances are known to be more unstable than the stationary crossflow disturbances. Traveling disturbances are sensitive to freestream turbulence level, which is relatively low at aircraft flight altitudes. Therefore, traveling disturbances are considered to be much less relevant as compared to stationary disturbances, which are directly induced by surface roughness. Here, the results of the NPSE computations are presented, which show that the growth of traveling disturbances is also suppressed by introducing smaller-wavelength stationary crossflow disturbances (i.e., DRE).

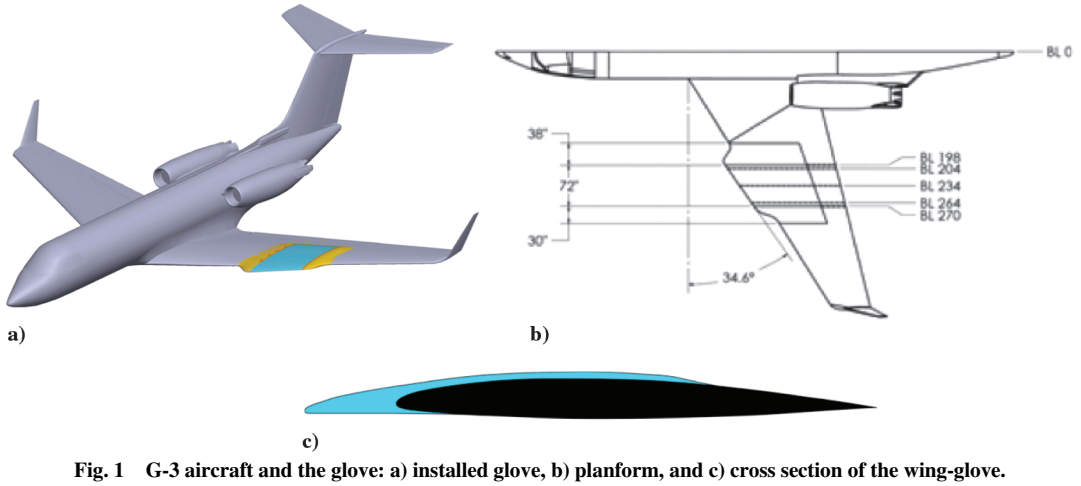

Fig. 1 G-3 aircraft and the glove: a) installed glove, b) planform, and c) cross section of the wing-glove.

II. Computational Test Article

A. Laminar-Flow-Glove Design

The goal set by the ERA Project was to demonstrate the DRE technology for a leading-edge sweep in excess of 30 deg and chord Reynolds numbers that are characteristic of midrange transport aircraft (i.e., Re_c up to 30×10^6). The design of a laminar-flow glove for the G-3 aircraft was described in [28]. The glove has a leading-edge sweep of about 34.6 deg compared to 31.7 deg for the original wing. Figure 1 shows the glove as installed on the G-3 aircraft wing. The glove width is 6 ft and the midspan chord length, including the glove, is 14.5 ft. The Mach-number range of interest is 0.66–0.75, with cruise section C_L of approximately 0.5. The chord Reynolds numbers in the range of 15×10^6 to 30×10^6 could be achieved within the designed flight envelope. One of the objectives of the experiment was to demonstrate that DRE could delay transition by 50% as compared to the NLF case.

The flow conditions for the present computations are $M = 0.75$, $H = 38,840$ ft, angle of attack $= 3.5$ deg. The resulting glove midspan chord Reynolds number is 24.2×10^6; however, for convenience, it is identified as 24×10^6 elsewhere in the paper. In [29], both structured-grid (OVERFLOW, [31]) and unstructured-grid (FUN3D[¶]) Navier–Stokes codes were used to compute the aircraft flowfield including the wing glove. Figure 2 shows the upper-surface C_p distribution in the glove region. The three vertical lines ($Y = 204$, 234, and 264 in.) in the plot indicate the distance from the center of the aircraft fuselage. The three spanwise lines indicate relative distance X/C from the leading edge, the line denoted $X/C = 0.6$ being slightly ahead of the shock. In these computations, turbulent flow was assumed everywhere (and is computed using the Spalart–Allmaras model) except on the glove upstream of the shock where the flow is assumed to be laminar. It should be noted that the isobars in the glove region have sweep angles smaller than the constant X/C lines, particularly at larger distances from the leading edge. This unsweeping of the isobars has an important effect on boundary-layer stability, as discussed in [29] and summarized as follows.

B. Boundary-Layer Mean Flow

Figure 3 shows the C_p distribution along the $Y = 234$ in. butt line. The favorable pressure distribution on the upper surface assures that the TS instability is minimized and crossflow instability is present due to the glove sweep. The upper-surface-pressure distribution along with the airfoil cross section along $Y = 234$ in. is used in the laminar boundary-layer code [32] under the infinite-swept-wing assumption, and the resulting mean-flow profiles will be used in the analyses presented in the next section. However, it is important to point out the differences between this mean flow computed under the infinite-swept-wing assumption and the fully 3-D mean flow present in the midspan region of the glove. The 3-D boundary-layer flow on the glove was extracted from the FUN3D and OVERFLOW viscous computations. A quantity that can be used to gauge the strength of crossflow instability is the crossflow Reynolds number defined as

$$R_{\mathrm{cf}} = \frac{W_{\max}\delta_{0.1}}{\nu_e}$$

in which $W_{\max}$ is the maximum crossflow velocity, $\delta_{0.1}$ is the distance from the wall where the crossflow velocity reduces to 10% of its maximum value, and ν_e is the kinematic viscosity at the boundary-layer edge.

Figure 4a shows a comparison of R_{cf} computed from the boundary-layer code, under infinite-swept-wing assumption and full 3-D solution from the two Navier–Stokes codes. For the latter computations, boundary-layer profiles were extracted from the steady laminar Navier–Stokes solutions to obtain the maximum crossflow velocity and the crossflow length scale at each station. The values of crossflow Reynolds numbers computed from FUN3D and OVERFLOW solutions are quite close, except that the former gives a nonsmooth distribution, as the boundary-layer profiles are linearly interpolated from the tetrahedral grid in this case, whereas no interpolation was required for the case of the OVERFLOW solution. Figure 4b shows inviscid streamlines computed from the FUN3D solution. A streamline computed from the OVERFLOW solution is also shown for comparison, and the results from the two Navier–Stokes codes essentially coincide. It is clear that the full 3-D mean flows from the FUN3D and OVERFLOW codes yield much lower values of R_{cf}, particularly away from the leading edge, and this is because the unsweeping of the isobars helps reduce the crossflow component of the velocity as compared to the infinite-swept assumption. The much lower values of crossflow will then result in much reduced growth rates for the crossflow instability. This is shown in Fig. 5, in which N factors are plotted for stationary crossflow disturbances of fixed spanwise wavelengths. These N factors are computed using quasi-parallel linear-stability theory (LST), as implemented in the LASTRAC code [33]. The mean flows used in these analyses are computed using the boundary-layer code and the FUN3D code. The boundary-layer solution, under the infinite-swept assumption, yields a maximum N factor of about 20, which reduces to about 12 for the mean flow using FUN3D. This reduction in N factor is expected because of a substantial reduction in the R_{cf} shown in Fig. 4a. A similar reduction in the N factor was noted when mean flow from the structured-grid OVERFLOW code was used.

The preceding results show that the as-designed G-3 glove boundary layer is much more stable than the boundary layer under the infinite-swept assumption using the same streamwise pressure distribution. However, to simplify the computations of nonlinear disturbance evolution, the infinite-swept-wing boundary-layer solution was used in

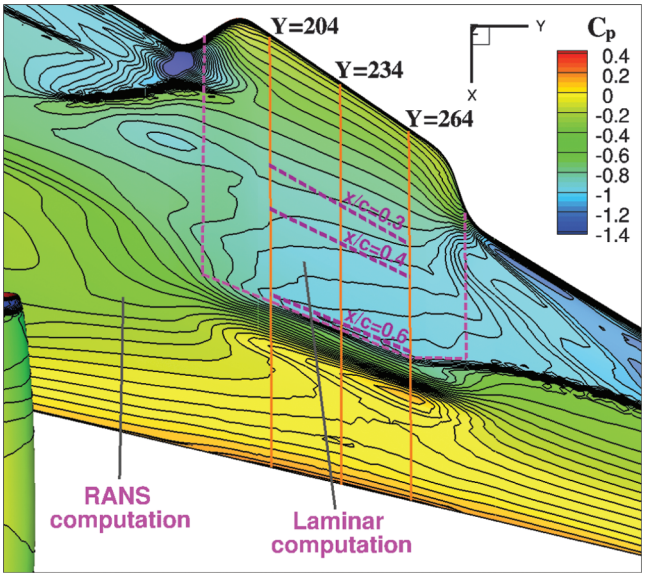

Fig. 2 Upper-surface C_p distribution computed using FUN3D.

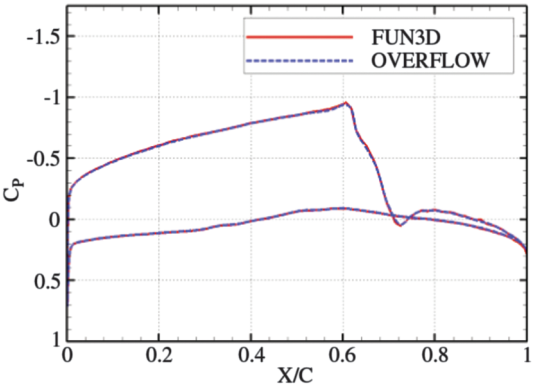

Fig. 3 Computed C_p ($Y = 234$ in.) using FUN3D and OVERFLOW.

[¶]Data available online at http://fun3d.larc.nasa.gov/ [retrieved December 2012].

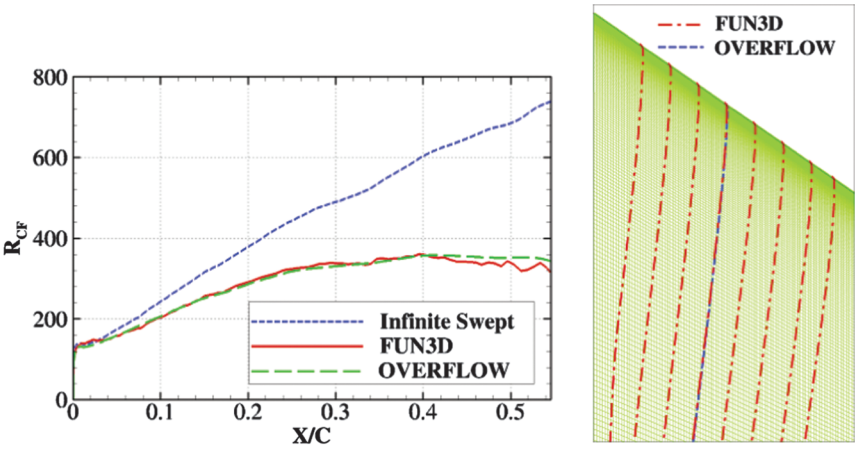

Fig. 4 Crossflow Reynolds number and inviscid streamlines.

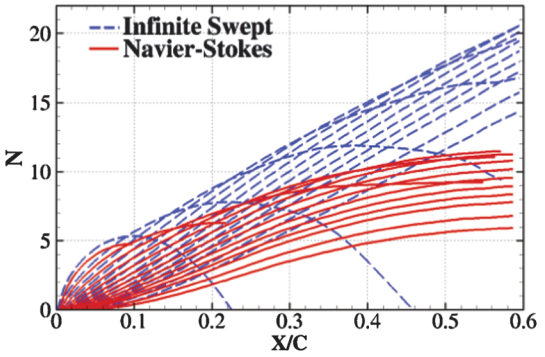

Fig. 5 *N* factors for various disturbance wavelengths using LST.

the computational results presented as follows. Because of the substantially higher linear growth in the infinite-swept case, transition assessment in this context presents a more stringent test for the effectiveness of DREs in comparison with the actual boundary-layer flow over the glove. The reader should note that the chord Reynolds number for the freestream conditions given previously is 24×10^6. In the next section, the stability results for two additional Reynolds numbers, namely, 17×10^6 and 30×10^6, are presented, but the boundary-layer mean flows for these cases were computed with the same C_p shown in Fig. 3 by simply changing the freestream Reynolds number.

III. Nonlinear Computations and Secondary-Instability Analysis

A. Selection of Target and Control Modes

Calculations were first performed to determine the wavelength of the most amplified stationary (zero frequency) crossflow disturbances, whose growth needs to be suppressed to delay transition. Because these are the targets of the DRE control, instability associated with this wavelength is designated as the target mode. The determination of the target-mode wavelength is done by performing a linear-parabolized-stability-equation (LPSE) analysis, which includes surface curvature and nonparallel effects. Figure 6 presents the LPSE results for three Reynolds numbers (17×10^6, 24×10^6, and 30×10^6). For demonstration purposes, the target-mode wavelengths were selected to be 10, 8, and 7 mm for the three Reynolds numbers, respectively. The *N* factors computed using the LPSE for these spanwise wavelengths, and others, grow to large numbers between 11 and 20, approximately. The stationary crossflow disturbances associated with these wavelengths are the target modes for this control study and the subject of control using DRE. The results in Fig. 6 also show *N* factors for smaller-wavelength disturbances. For example, wavelengths of 2.67 and 4 mm reach the maximum *N* factors of 4 and 6.5, respectively, for $Re_c = 24 \times 10^6$. A wavelength of 4 mm was selected as the control mode because the 2.67 mm mode was found to have a relatively weak effect on the target mode. The control modes with wavelengths of 5 and 2.33 mm are selected for the Reynolds numbers of 17×10^6 and 30×10^6, respectively. Table 1 lists the corresponding Reynolds number, and the target- and control-mode wavelengths.

B. Nonlinear Evolution of Stationary Crossflow Disturbances with and Without DRE Control

NPSEs, as implemented in LASTRAC, were used to study the evolution of target modes with and without the control modes. For an infinite-swept wing, the NPSE solution for a general nonlinearly developing traveling crossflow wave with a fundamental frequency f and fundamental spanwise wave number β is given by

$$\phi(x, y, z, t) = \sum_m \sum_n \hat{\phi}(x, y, m, n) \times \exp\left(i \int_{x_0}^{x} \alpha_{mn}(\xi)\, \mathrm{d}\xi + in\beta z - im2\pi f t\right) \quad (1)$$

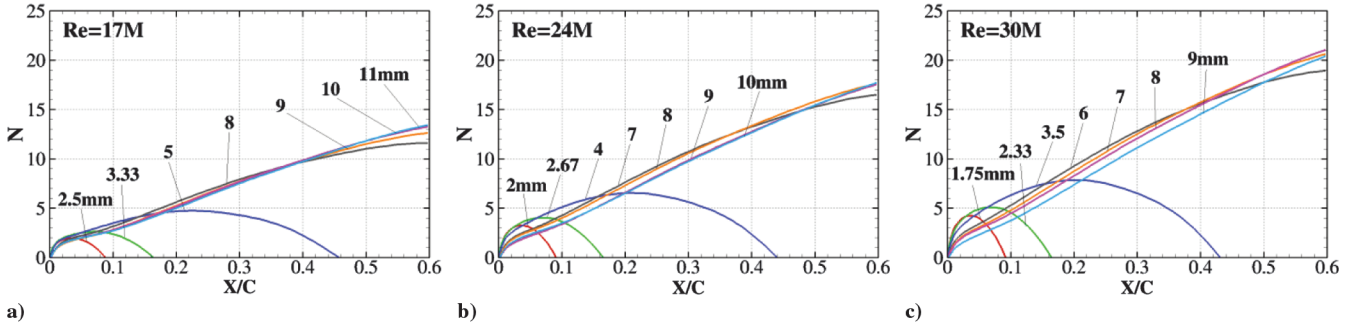

Fig. 6 *N* factors using LPSE for various Reynolds numbers: a) 17×10^6, b) 24×10^6, and c) 30×10^6.

Table 1 List of corresponding target- and control-mode wavelengths and Reynolds number

$Re_c \times 10^{-6}$	Target-mode wavelength, mm	Control-mode wavelength, mm
17	10	5
24	8	4
30	7	2.33

in which ϕ represents any perturbation field variable; x, y, and z are, respectively, the chordwise, wall-normal, and spanwise surface coordinates; and α_{mn} is the streamwise wave number of Fourier component (m, n). Resolving a general nonlinear perturbation wave accurately requires many Fourier modes (m, n), which makes the computation of traveling waves more time consuming than that of stationary waves. However, to begin with, we present results for purely stationary modes, in which case $f = m = 0$, and Eq. (1) becomes

$$\phi(x, y, z) = \sum_n \widehat{\phi}(x, y, n) \exp\left(i \int_{x_0}^{x} \alpha_{0n}(\xi)\, d\xi + in\beta z \right) \quad (2)$$

In the computations discussed next, both target and control modes are initiated at the lower-branch neutral location of the target mode. The initial mode shapes for the target and control modes were determined from the LPSE analysis. These modes were assigned some arbitrary initial amplitude, which was very small for the target mode and relatively larger for the control mode. This is because the DRE control will induce relatively large amplitude of the smaller-wavelength control mode as compared to the target mode, which is induced by the natural distributed surface roughness. Different initial amplitudes of the target modes are linked to the surface quality (e.g., polished vs painted), and different initial amplitudes of the control mode to the height and diameter of the DREs. A quantitative analysis for a specific experimental configuration would require the determination of boundary-layer receptivity to the actual shape, height, and distribution of the roughness. Lacking a priori information concerning the roughness definition, the consideration of the receptivity phase is avoided in the current analysis, which makes the present results qualitative in nature. It is clear that an analysis using other methods, such as the linear-receptivity theory or DNS of the natural and imposed surface roughness, will be required to draw definitive conclusions.

Throughout this paper, the word "amplitude" will frequently be used; therefore, it is necessary to clarify its meaning here at the outset. Unless otherwise stated, the amplitude of the perturbation at a location on the wing is defined as the ratio of the local maximum of the chordwise perturbation velocity to the global freestream velocity. Perturbation quantities are often decomposed into spanwise Fourier modes. The modal amplitude of a Fourier mode, consistent with the preceding definition, is the maximum of its chordwise component normalized by the global freestream velocity.

The results for the evolution of various modes in a nonlinear computation for $Re_c = 24 \times 10^6$ are described first. To initiate the nonlinear computation, the mode shape is first computed for the target mode of wavelength 8 mm using LPSE. The chordwise-velocity component for this mode is assigned an initial amplitude of 10^{-4} (i.e., 0.01% of the freestream velocity). For stationary crossflow computations, the number of Fourier modes used in the spanwise direction is 40 [i.e., $-40 < n < 40$ in Eq. (2)]. Figure 7a presents the results for the case without control. The primary mode (0, 1) initially follows the LPSE result until its harmonics grow to significantly enough amplitudes for the primary mode to saturate, as indicated by the flattening out of the amplitudes in Fig. 7a. It can be seen that the disturbance energy cascades into the harmonics (0, 2), (0, 3), etc. The mean-flow distortion (0, 0) mode also gains significance, and it attains amplitude equivalent to the first harmonic (i.e., 0, 2) mode. These results are similar to the nonlinear crossflow-disturbance evolution computed in [12] for a canonical problem and in [13] for a low-speed swept-wing flow. The results for the case with DRE control using a control wavelength of 4 mm [(0, 2) mode] are shown in Fig. 7b, with an initial amplitude for the control mode of 0.015 (i.e., 1.5% of the freestream velocity). Note that, in contrast with the results in Fig. 7a, an initial amplitude of (0, 2) mode is much higher than the (0, 1) mode by specification. It can be seen that the control mode initially grows, but eventually decays within a short chordwise distance, as expected from the LPSE results. The target-mode growth is delayed, as discussed in detail in the following paragraphs. Here, one should note that, after a period of decay, the control mode picked up again further downstream as a harmonic of the target mode, which, by then, had attained a large amplitude.

Figure 8 shows the results of a stationary crossflow vortex with and without control at $x/c = 0.35$. Two spanwise periods are shown. The

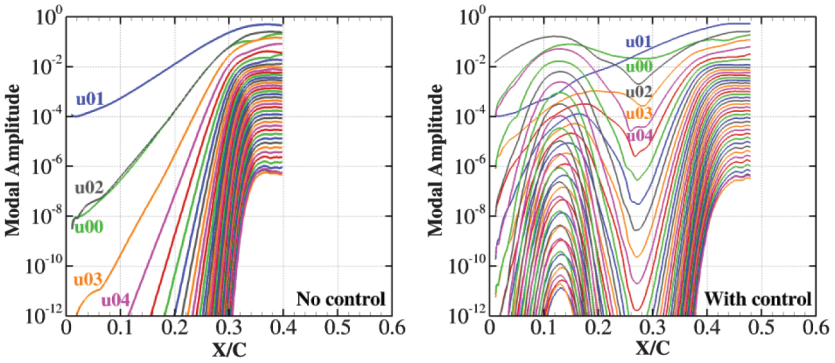

a) No control b) With control

Fig. 7 Evolution of modal amplitudes with and without control for $Re_c = 24 \times 10^6$.

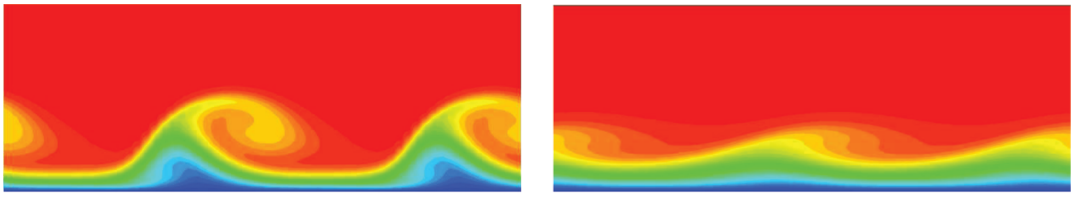

a) No control b) With control

Fig. 8 Stationary crossflow vortices showing chordwise velocity at $X/C = 0.35$ for the case in Fig. 7.

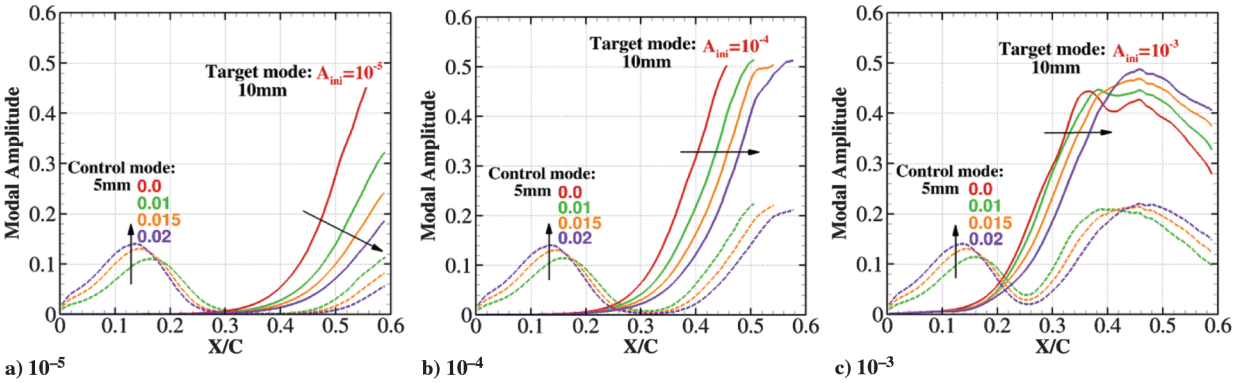

a) 10^{-5} b) 10^{-4} c) 10^{-3}

Fig. 9 NPSE results with and without control for $Re_c = 17 \times 10^6$.

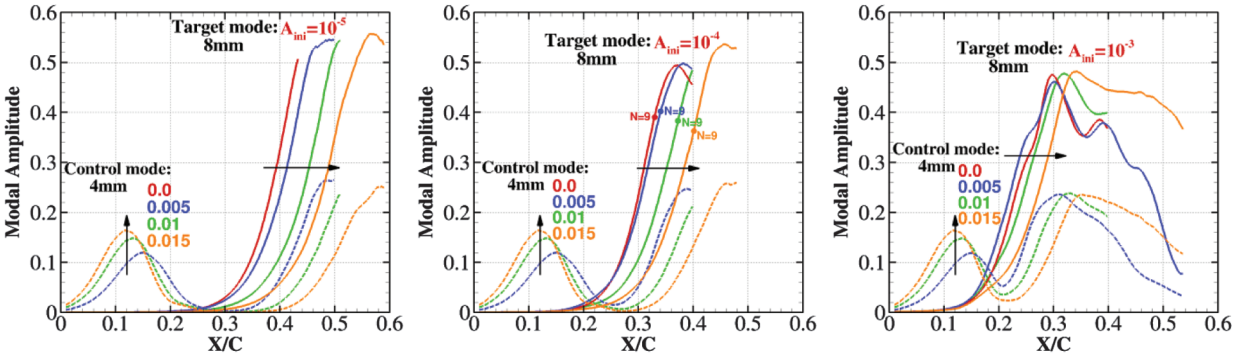

a) 10^{-5} b) 10^{-4} c) 10^{-3}

Fig. 10 NPSE results with and without control for $Re_c = 24 \times 10^6$.

introduction of the small-wavelength control mode suppresses the development of the crossflow vortex, which can be clearly seen in Fig. 8b when compared to Fig. 8a, implying that the transition induced by the stationary crossflow mechanism will be delayed.

The results for the crossflow-disturbance evolution for three different Reynolds numbers (17×10^6, 24×10^6, and 30×10^6), with and without DRE control, are shown in Figs. 9–11. In this case, only the amplitudes of the target and control modes are shown. The target modes were assigned three different amplitudes of 10^{-5}, 10^{-4}, and 10^{-3}, qualitatively representing ultrapolished, polished, and painted surfaces, respectively. The initial amplitudes of the control modes were selected as 0 (i.e., no control), 0.005, 0.01, and 0.015. For $Re_c = 17 \times 10^6$, additional computations with a control amplitude of 0.02 were performed. The target-mode growth was progressively delayed further downstream with increasing control amplitude in all cases.

In the results shown in Figs. 9–11, the saturation amplitude of the target mode reached in excess of 0.5 (i.e., 50%). In the low-speed case analyzed in [13], the fundamental mode saturated at only about 20%. In that case, the amplitude was based on the ratio of the maximum perturbation local velocity to the boundary-layer-edge velocity in the inviscid streamline direction. If the freestream-velocity-based amplitude of 50% in the present analysis is converted to the boundary-layer-edge-velocity-based amplitude, the value drops to approximately 40%, mainly because the boundary-layer-edge velocity is larger than the freestream velocity. This conversion enables comparisons to be made between the two cases. In the present high-speed case, the saturation amplitude is approximately twice as large as it was in the low-speed case. If one assumes that transition will occur when the disturbance amplitude exceeds some fixed amplitude, say 0.25, then transition locations for the no control and control (amplitude = 0.015) cases can be estimated from these results, and are given in Table 2 for the three Reynolds numbers and the three initial amplitudes of the target modes. Note that the actual value of amplitude chosen is not particularly import for evaluating relative changes in transition location as long as it is sufficiently large to

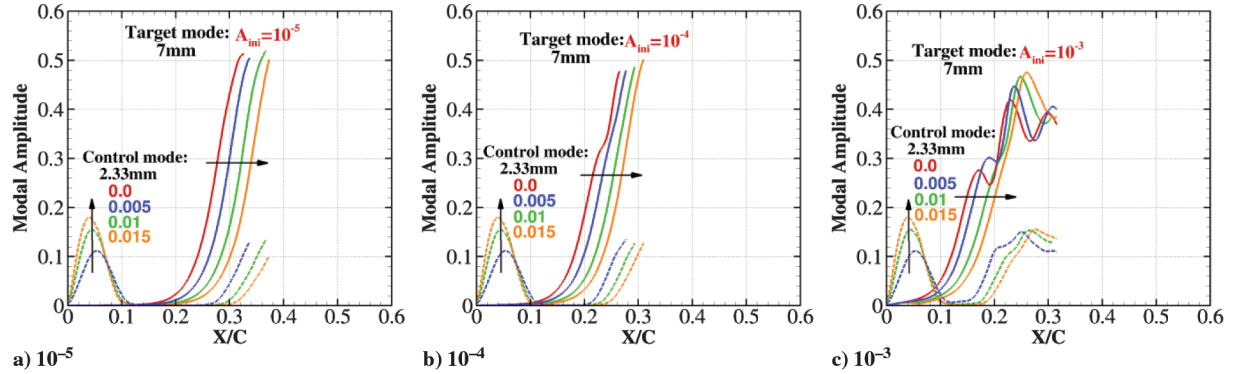

a) 10^{-5} b) 10^{-4} c) 10^{-3}

Fig. 11 NPSE results with and without control for $Re_c = 30 \times 10^6$.

Table 2 Effect of DRE-based control (amplitude = 0.015) on delay in boundary-layer transition based on final target-mode amplitude of 0.25

$Re_c \times 10^{-6}$	A_{ini}	$(X/C)_{tr}$	$(X/C)_{tr}$ with control	Increment, %
17	10^{-3}	0.281	0.306	9
	10^{-4}	0.378	0.434	15
	10^{-5}	0.493	0.591	20
24	10^{-3}	0.234	0.275	17
	10^{-4}	0.303	0.374	24
	10^{-5}	0.385	0.479	24
30	10^{-3}	0.157	0.207	32
	10^{-4}	0.212	0.266	26
	10^{-5}	0.271	0.333	23

Table 3 DRE-based control for $Re_c = 17 \times 10^6$, using initial amplitude of 0.02 and transition location estimated using final target-mode amplitude of 0.25

A_{ini}	$(X/C)_{tr}$	$(X/C)_{tr}$ with control	Increment, %
10^{-3}	0.281	0.324	15
10^{-4}	0.378	0.455	20
10^{-5}	0.493	0.631	28

support secondary instabilities. It can be seen that, except for the lowest Reynolds number and the highest initial amplitude of the target mode, DRE control (using initial amplitude = 0.015) moves transition location (X/C) by 20–25%. The next section reports the estimated transition locations based on the secondary-instability analysis. Here, one should note that transition delay using an initial amplitude of 0.015 for $Re_c = 17 \times 10^6$ is smaller than 20%. It requires an initial amplitude of 0.02 to delay transition beyond 20% in this case (see Table 3). No attempt has been made to optimize the results with respect to the control-mode wavelength, and the results in Tables 2 and 3 are likely to change if an optimization study were to be performed. However, it is felt that such a study would not add value without including the critical step of boundary-layer receptivity to DRE and surface roughness.

C. Secondary Instability of the Target and Control Modes

As the stationary crossflow-vortex amplitude increases, the nonlinear interactions among the many harmonics of the disturbance cause the crossflow vortex to reach large-amplitude quasi-saturated state, which leads to the appearance of strong shear layers as can be inferred from the results in Fig. 8a. The crossflow vortex is now susceptible to secondary instability similar to that in the case of large-amplitude Görtler vortices [34,35]. The secondary instability is similar to the primary instability in that it is also an unstable perturbation to some mean-flow state. The main difference is that, for a primary-instability wave, the mean flow varies strongly in the wall-normal direction only, but for a secondary-instability wave, the mean flow also varies strongly in the spanwise direction; the streamwise variation in both cases is considered to be weak. The mathematical formulation of the former leads to an eigenvalue problem of a set of ordinary differential equations depending on a single spatial variable, whereas that of the latter gives rise to an eigenvalue problem of a set of partial differential equations depending on two spatial variables.

For the particular problem of secondary instability of stationary crossflow vortices, the mean flow varies strongly in the wall-normal direction, and, owing to the infinite-swept assumption, is periodic in the spanwise direction. Along the crossflow-vortex axis, the mean flow varies slowly, and, therefore, a parallel assumption can be made to ignore the mean-flow changes so that an ansatz can be used to factor out the oscillatory component of the secondary-instability wave in this direction. However, a problem unique to this flow configuration is that the direction of the crossflow-vortex axis is not orthogonal to the spanwise direction. This somewhat complicates the mathematical formulation. To get around this problem, a nonorthogonal coordinate system was devised (see [36,37]) that properly enforces the periodicity in the spanwise direction and the slow variation in the vortex-axis direction, resulting in the correct chordwise (i.e., in x direction) secondary-instability growth rate.

The secondary-instability code used in the current analyses has been validated against solutions of NPSE and DNSs based on a mean flow that is invariant along the vortex axis and a small initial amplitude perturbation at inflow. The agreement was excellent.

In the numerical computations, fourth-order finite differences were used in the wall-normal direction, and the Fourier spectral method was used in the spanwise (periodic) direction with typically 121 and 32 points, respectively. Given that there are five equations in this problem, the total number of degrees of freedom of the resulting discretized system is $5 \times 121 \times 32 = 19,360$. Grid convergence is confirmed by carrying out the eigenvalue computations using more grid points in each direction for selected points in the parameter space of the problem.

A typical secondary-instability N factor computation procedure can be summarized (see [36,37] for details) as follows:

1) Using the Arnoldi method, a thorough temporal eigenvalue search at a few selected streamwise stations was carried out to identify the relevant secondary-instability modes and their frequency ranges.

2) A suitable representative subset of secondary-instability modes was chosen to span the relevant frequency range. Each of these temporal eigenvalues was subject to iterations toward a spatial eigenvalue by fixing the real part of the eigenvalue (complex frequency) and changing the complex wave number until the imaginary part of the frequency became smaller than a preset tolerance. The inverse Rayleigh iteration method was employed in this step.

3) With each selected eigenvalue from the previous step as an initial guess, the eigenvalue computations were marched both upstream and downstream in the chordwise direction to cover the entire chordwise range of interest. Finally, N factors are computed from the eigenvalues.

Secondary-instability computations were performed for the three Reynolds numbers using the target-mode amplitude of 10^{-4}. Various control amplitudes between 0 and 0.015 were used. Figure 12 presents the secondary N factor results for the target and control modes.

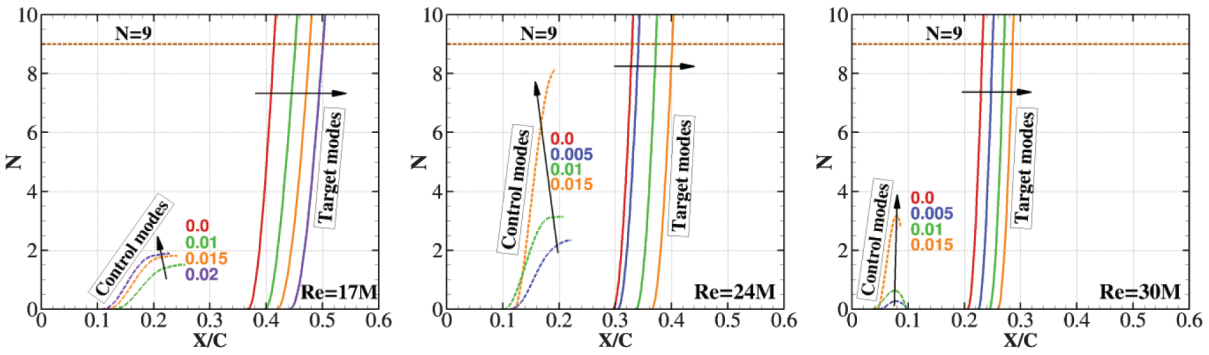

a) 17 million b) 24 million c) 30 million

Fig. 12 Secondary N factors for target-mode amplitude of 10^{-4}.

Table 4 Effect of DRE control (amplitude = 0.015) on delay in boundary-layer transition based on secondary-instability N factor of 9, for initial target-mode amplitude of 10^{-4}

$Re_c \times 10^{-6}$	$(X/C)_{tr}$	$(X/C)_{tr}$ with control	Increment, %
17	0.414	0.500	21
24	0.329	0.401	22
30	0.232	0.286	23

The secondary-instability N factors for the target mode rise very sharply for all control amplitudes and Reynolds numbers. If the secondary instability $N = 9$ is selected to indicate the onset of transition, then the delay in boundary-layer transition because of the DRE could be computed (Table 4). It can be seen that transition delay is between 20 and 23% for the three Reynolds numbers. Because the N factor curves are essentially parallel, the percent change in transition will remain the same regardless of the value of the N factor selected to indicate transition onset. It is also noted that transition delay predicted by the secondary-instability analysis is much more consistent for the three Reynolds numbers as compared to predictions based on fixed amplitude in Table 2.

The secondary N factors for the control modes are also presented in Fig. 12. For the 1.7×10^7 Reynolds-number case, the maximum N factors are approximately the same (just under 3) regardless of initial amplitudes. For the 2.4×10^7 Reynolds-number case, the maximum N factors are strongly dependent on the initial amplitudes, and the largest of these reaches approximately 8.5. For the highest Reynolds-number case of 3.0×10^7, the initial amplitude dependency of the maximum N factors is strong, but the maximum N factor reached is only approximately 3. This apparent lack of trend in the secondary-instability N factors for the control mode should not come as a surprise, because the Reynolds number is not the only parameter that is different in these three cases. For the first two cases, the control-mode wavelength is half that of the target mode, whereas for the last case, the control-mode wavelength is only one-third that of the target mode. Different control-mode wavelengths may give rise to different values of secondary N factors and may also influence the nonlinear growth of the target modes as noted previously.

One of the potential problems of the DRE control is that, if too much control is introduced, the control mode itself may lead to transition by attaining large-enough amplitudes and, hence, becoming susceptible to secondary instability [24]. The secondary-instability-analysis results presented previously in Fig. 12b for the 4 mm control mode with an initial amplitude of 0.015 (the largest used for the control mode) show that the maximum N factor of secondary instability reaches approximately 8.5. A secondary-instability analysis using NPSE needs to be performed to determine whether this instability will lead to transition. To do this computation, the linear secondary-instability mode for the most amplified frequency of 95 kHz at $X/C = 0.12$ is Fourier decomposed in the z direction into different $n\beta$ modes [see Eq. (1)], and used as inflow conditions (along with the stationary modes) for the NPSE analysis. Three different initial amplitudes for the secondary disturbances are used, namely, 10^{-6}, 10^{-5}, and 10^{-4}. The amplitude of the stationary control mode is fixed at 0.015. As shown in Fig. 13, with the two smaller initial amplitudes, the secondary instability grows and dies without causing transition. With the third, higher initial amplitude, the secondary-instability amplitudes exhibit some oscillatory behavior; however, an examination of the rms contours of the streamwise perturbation velocity shows no indication of the flow breaking down to smaller scales. Thus, transition due to the control mode is not expected in this case either.

The secondary-instability results presented herein suggest that the DRE could delay stationary crossflow-induced transition by about

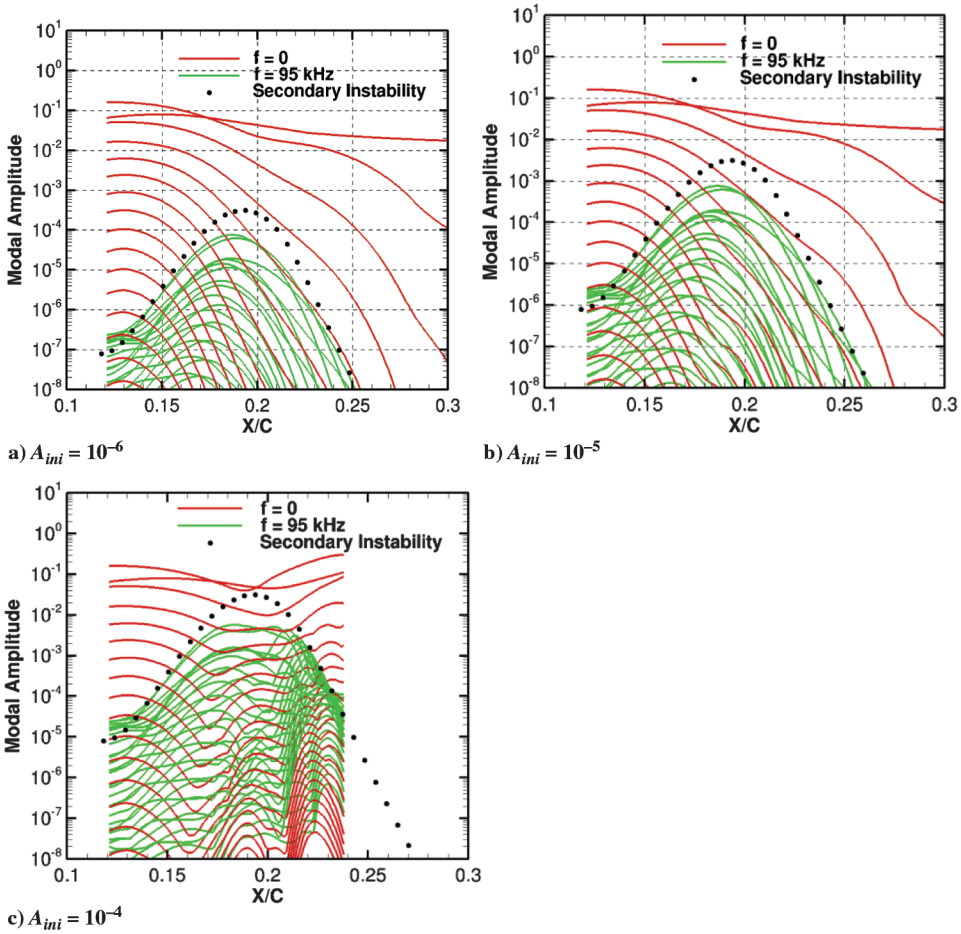

Fig. 13 Comparison of linear secondary-instability and NPSE (lines).

20% for all three Reynolds numbers as compared to the no-control swept-wing NLF case. The secondary-instability analysis also yielded interesting results on the characteristics of secondary-instability modes, but that discussion is deferred to a later section, as their characteristics are not directly related to the main theme of the paper. The question of DRE-based control in the presence of traveling crossflow disturbances is considered first.

D. Effect of DRE on Traveling Crossflow Disturbances

It is well known that traveling disturbances grow much more than the stationary ones, and, if excited at a sufficiently high amplitude, would dominate laminar–turbulent transition in swept-wing flows. Based on the experimental data of [38,39], it was argued in [40] that transition is caused by stationary disturbances when $Tu \sim 0.02\%$, and dominated by traveling instability waves when $Tu \sim 0.15\%$. Because the turbulence level at aircraft flight altitudes is low, the in-flight swept-wing transition is expected to be caused by surface-roughness-induced stationary crossflow disturbances, which can then be controlled using the DRE. By performing NPSE computations, it is shown here that the DRE could also delay the growth of traveling crossflow disturbances if present in the boundary layer.

As noted earlier, the NPSE solution for a general nonlinearly developing traveling crossflow wave of a fixed frequency f and spanwise wave number β is given by Eq. (1). Resolving a general nonlinear perturbation wave accurately requires many Fourier modes (m, n), which makes the computation of traveling waves more time consuming than that of stationary waves. However, if a nonlinear perturbation develops from a single small-amplitude wave initialized as Fourier mode (1, 1), the only harmonics that are nonlinearly generated as the wave amplitude grows are those on the diagonal of the (m, n) plane, that is, modes (n, n); all other off-diagonal modes for which $m \neq n$ are 0. Consequently, a coordinate transformation can be made as follows:

$$Z = z - (2\pi f/\beta)t \tag{3}$$

that is, the new coordinate system travels spanwise with the spanwise phase speed of the perturbation. Upon substitution of Eq. (3) into Eq. (1), one has

$$\phi(x, y, Z) = \sum_n \widehat{\phi}(x, y, n) \exp\left(i \int_{x_0}^{x} \alpha_{0n}(\xi)\, \mathrm{d}\xi + in\beta Z \right) \tag{4}$$

Therefore, the problem now becomes one of stationary wave, resulting in an order of magnitude speed up in computational turnaround. For example, if a nonlinearly evolving traveling crossflow vortex requires 48 spatial Fourier modes to resolve in a traveling frame of reference, it will require 48×48 spatial and time Fourier modes to resolve the wave in the fixed frame of reference, because these Fourier modes now lie along the diagonal of (m, n) space, and Eq. (1) must be used to represent the perturbation. The coordinate transformation works best and results in the savings of memory and time when only a single traveling crossflow vortex is initialized; however, it also works in some specific cases, in which both stationary and traveling crossflow vortices are present as exemplified in the following case.

If a stationary mode of shorter wavelength is introduced to control the traveling mode, then a transformation of the form given by Eq. (3) will not result in a stationary flowfield. However, because the maximum amplitude of the control mode remains relatively small, fewer Fourier modes are required to accurately represent it. By applying the transformation in Eq. (3), the traveling target mode becomes stationary, and the stationary control mode becomes a traveling mode. A larger number of modes are used in n to resolve the target mode, whereas fewer modes are used in m, mainly for the control mode. Equation (1) will be used in this case, with m much smaller than n.

Using the preceding approach, NPSE computations were performed for $Re_c = 24 \times 10^6$, for which the linearly most unstable traveling crossflow-instability mode has a frequency of approximately 1 kHz and a spanwise wavelength of 12 mm (the target mode). The stationary control mode has a spanwise wavelength of 4 mm (one-third of the target mode). The NPSE computation is carried out in the spanwise traveling coordinate system as explained previously; the target mode becomes stationary, and the control mode appears to have a frequency of −3 kHz. It can be seen in Fig. 14 that the linear N factors of the 12 mm target mode and the 4 mm control mode computed in the stationary frame and the traveling frame gave rise to the same results in each case. Thus, the switch from a stationary frame to a traveling frame does not alter the stability properties of the perturbations being analyzed.

In the control case in which both stationary and traveling modes were present, the coordinate transformation also helped save resources. Suppose the computation was carried out in the fixed frame, then the harmonics generated by the target mode alone would align themselves along the diagonal of the (m, n) space, whereas those generated by the control mode alone would lie along the vertical axis $(0, n)$. Again, assuming that 48 modes are required to resolve the target mode, 48×48 spatial and time Fourier modes must be included in the computation. By using the moving frame of reference, the target-mode harmonics are transferred to the vertical axis $(0, n)$ with $n < 49$ and the control-mode harmonics, being initialized at (1, 3) in this case, now lie along $(m, 3m)$. As mentioned earlier, the control mode has a moderate amplitude, and, therefore, just five Fourier modes are sufficient to resolve it (i.e., $m < 6$); therefore, the total number of Fourier modes required is 48×5. There are, of course, nonzero off-diagonal Fourier modes in the (m, n) space that are generated via interactions of the control and target modes. However, in the chordwise range in which the control mode domi-

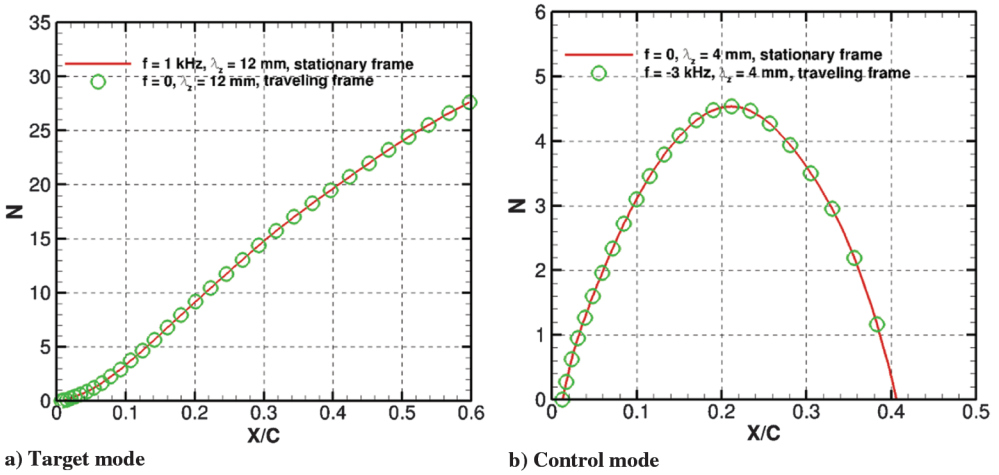

a) Target mode b) Control mode

Fig. 14 Effect of coordinate transformation Eq. (3) on traveling and stationary modes.

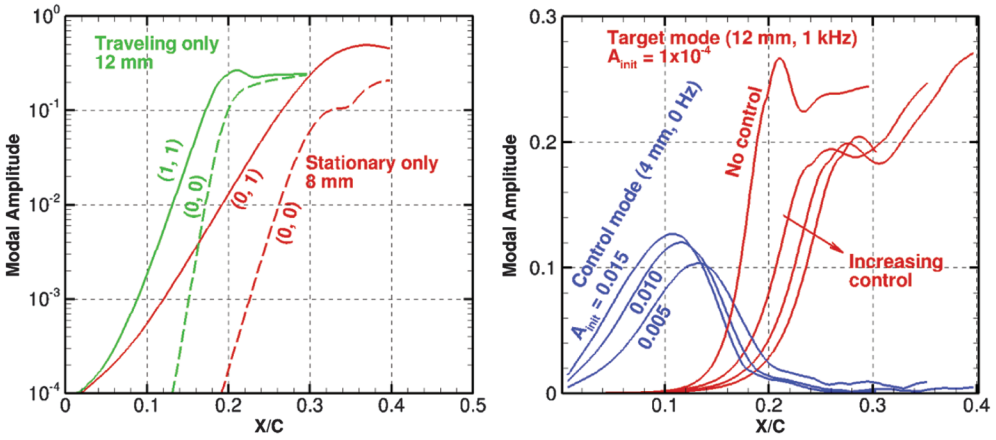

a) Evolution of stationary and traveling crossflow waves without control. Initial amplitude: 10^{-4}

b) Traveling crossflow wave with various controls, target mode initial amplitude: 10^{-4}

Fig. 15 Effect of control on traveling crossflow vortices.

nates, the target-mode amplitude is small, and the off-diagonal modes are of secondary importance.

Nonlinear computations for a 12 mm, 1 kHz traveling crossflow wave are first carried out in the absence of control. The evolution of the fundamental harmonic and the mean-flow correction are shown in Fig. 15a. For comparison, the same figure also shows the results of independent calculations pertaining to the evolution of the most amplified stationary mode with a wavelength of 8 mm. The number of Fourier modes used for the traveling-mode computation is 48, that is, $m = 0$ and $-49 < n < 49$, because it is done in the moving frame. [For presentation purposes, the fundamental traveling mode is still referred to as mode (1, 1) as if it were obtained in a stationary frame.] The initial amplitudes for both the stationary and traveling modes are 10^{-4}, and these computations are done independent of each other. It should be noted that the initial amplitude of the traveling mode would realistically be much lower, and it is only the higher subsequent growth that would help make the traveling mode more relevant. Consistent with the linear theory, the traveling wave has a larger growth rate as an examination of the amplitude-curve slopes will reveal. Interestingly, however, it is the stationary wave that reaches higher maximum amplitude than the traveling wave, approximately 50% for the former and less than 30% for the latter. The amplitudes of the mean-flow-correction components for both the stationary and traveling cases reach approximately 20%. The faster initial growth of the traveling wave also drives faster growth of its harmonics, enabling nonlinear effects to set in faster, causing the traveling wave to saturate earlier, and, hence, a smaller maximum amplitude results.

The effects of control are analyzed by using 5 Fourier modes in m and 48 Fourier modes in n. The 12 mm, 1 kHz target-mode initial amplitude is fixed at 10^{-4}, and three different amplitudes of the 4 mm control mode are used, namely, 0.005, 0.01, and 0.015. Figure 15b shows that, with increasing control amplitude, the rise of the target-mode amplitude is progressively delayed and its peak amplitude is also reduced, indicating that this control mechanism is very effective. This is consistent with the suggestion made in [41], based on a single low-Reynolds-number computation, that DRE control may also be applicable to traveling crossflow modes.

Figure 16 shows the mean velocity profiles at three selected streamwise stations in the presence of both the traveling target mode at the fixed amplitude (10^{-4}) and the stationary control mode at two amplitudes (0 and 0.015) (i.e., the case studied in Fig. 15b). The distortions to these profiles are chiefly caused by the control mode, because the target-mode amplitude is very small at these selected stations. The velocity profiles in the inviscid streamline direction show some velocity deficit near the boundary-layer edge, which gives rise to secondary instability (Fig. 13). The crossflow profiles show reduced maximum amplitude with increasing control, as noted previously for other configurations in [23,42], and this may be the main reason for the reduced target-mode growth.

Because freestream turbulence level in flight is low, it is reasonable to expect a much smaller initial amplitude of traveling disturbances than the surface-roughness-induced stationary crossflow disturbances. Therefore, another computation was performed using the initial amplitude of 10^{-6} for the traveling mode. The results are presented in Fig. 17a, which shows that the DRE provides an effective control of the traveling waves. The results are compared with the stationary target mode with wavelength of 8 mm and higher initial amplitude of 10^{-4} in Fig. 17b. The initial amplitude of the control

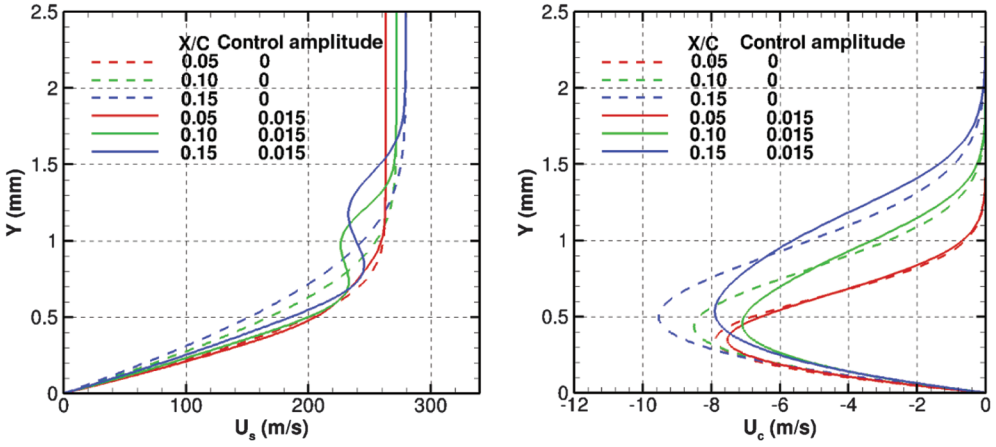

a) In inviscid streamline direction

b) In crossflow direction

Fig. 16 Mean-flow-velocity profiles with and without control mode.

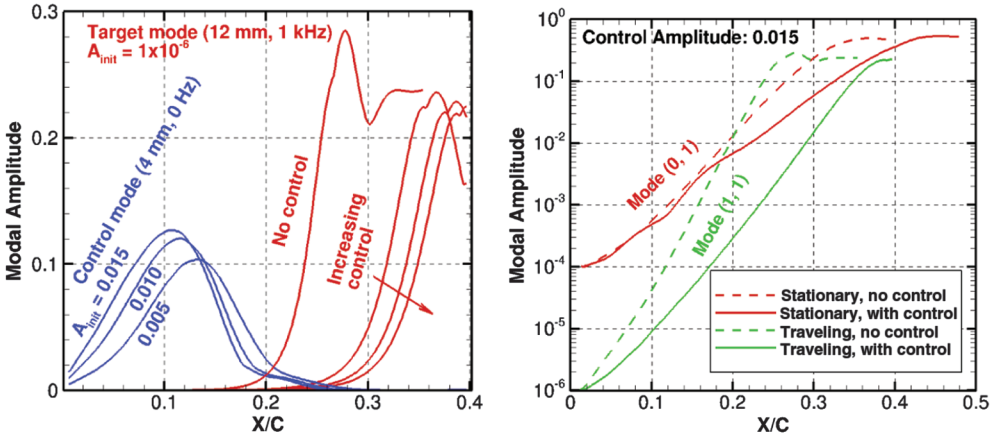

a) Traveling crossflow wave with various controls; target mode initial amplitude: 10^{-6}

b) Comparison of nonlinear evolution of stationary and traveling modes with and without control; initial amplitude of stationary mode = 10^{-4}, amplitude of traveling mode = 10^{-6}

Fig. 17 Effect of control on traveling crossflow vortices.

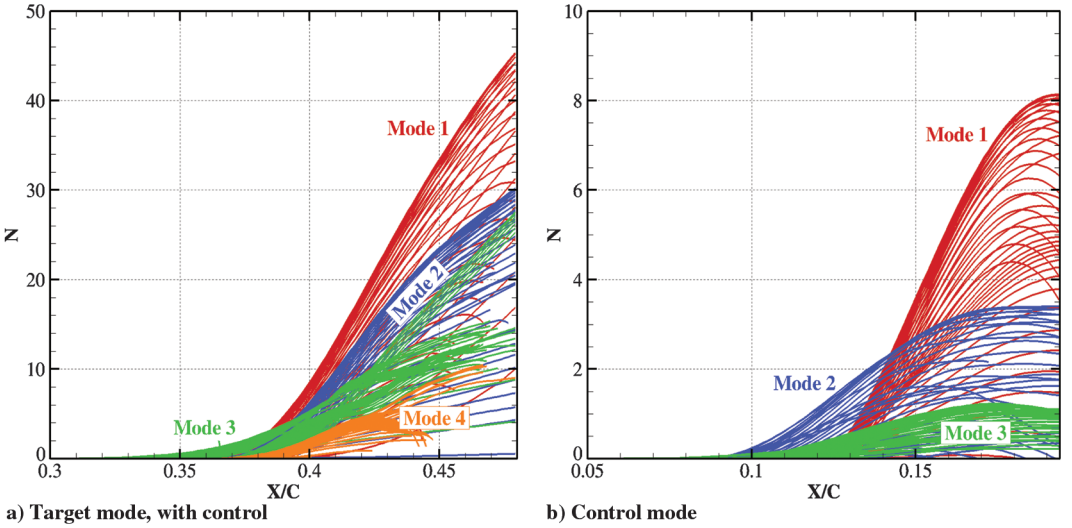

a) Target mode, with control

b) Control mode

Fig. 18 Secondary-instability N factors for target and control modes for $Re_c = 24 \times 10^6$.

mode is the same (0.015) in the two cases. Without any control, the traveling-crossflow-wave amplitude is already larger than that of the stationary wave at approximately 20% chord, even though the former's initial amplitude is 100 times smaller than that of the latter. With control, both stationary and traveling waves are suppressed. One should note that the two results are independently generated (i.e., stationary target mode only or traveling target mode only). There would, in fact, be interactions between the stationary and traveling modes if both were present simultaneously (cf. [12]). These interactions are difficult to track in the NPSE construct. Because both the stationary and traveling target modes reach large amplitudes and require a significant number of Fourier modes to resolve, no coordinate transformation will result in significant savings of computational resources.

E. Secondary-Instability Characteristics

In Sec. III.C, the secondary-instability analysis of stationary crossflow disturbances was performed to determine the effectiveness of DRE in controlling crossflow-induced transition. It was shown that the delay of transition in the presence of control mode is caused by the delay in the secondary-instability growth of the target mode. The analysis also yielded interesting results about the characteristics of secondary-instability modes, which are described here for both the target and control modes.

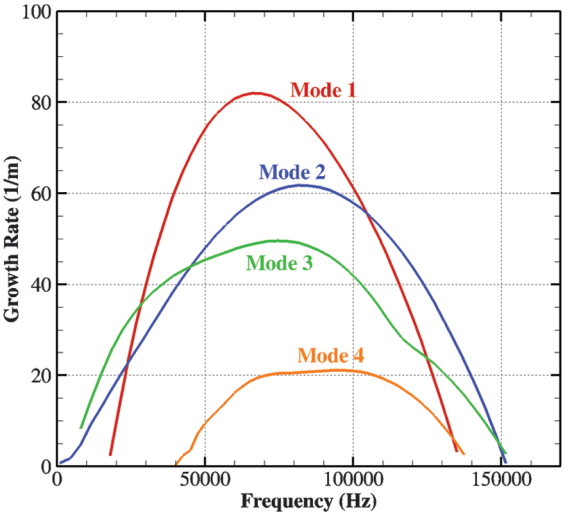

Fig. 19 Growth-rate spectra of secondary-instability modes shown in Fig. 18a; $X/C = 0.3856$.

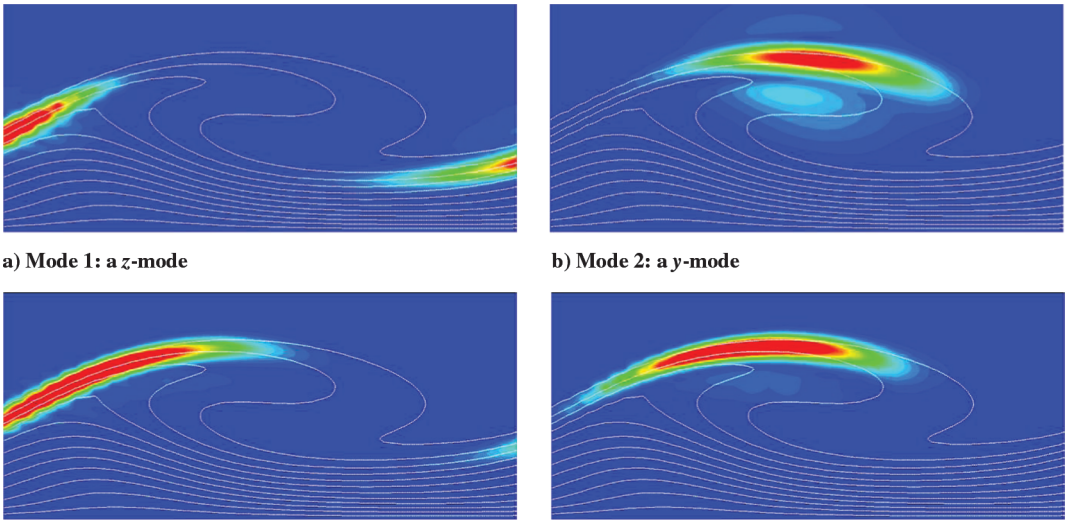

a) Mode 1: a z-mode b) Mode 2: a y-mode

c) Mode 3: a z-mode d) Mode 4: a y-mode

Fig. 20 Chordwise-velocity eigenfunctions for the four modes corresponding to Fig. 19.

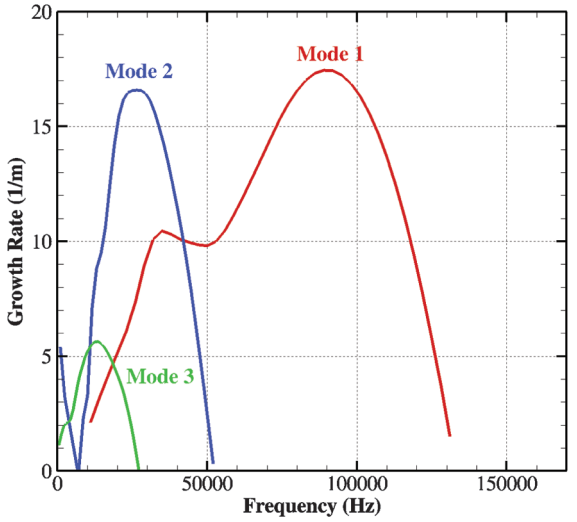

Fig. 21 Growth-rate spectra of secondary-instability modes shown in Fig. 18b; $X/C = 0.126$.

Figure 18 shows the N factor curves for the secondary-instability modes of various frequencies for the primary target and control wavelengths. Four significant secondary-instability modes are found for the target mode with initial amplitude of 10^{-4}, whereas three are found for the control mode with initial amplitude of 0.015. In each case, the most amplified mode is designated as mode 1, followed by mode 2, etc. The secondary instability of crossflow vortices was classified in [13] into two main categories (i.e., the y modes and z modes). The former is associated with the strong shear layer created by the velocity gradient in the wall-normal direction, and the latter with that in the spanwise direction. For the results shown in Fig. 18, mode 1 is a z mode for the target and a y mode for the control, that is, the two types of modes correlate, respectively, with the spanwise shear and wall-normal shear induced by the primary crossflow vortex. In the low-speed experiment of [43], z mode of secondary instability was detected.

The various secondary-instability-mode growth rates for the target mode are plotted in Fig. 19 as a function of frequency at a fixed streamwise station $X/C = 0.3856$. This location is a short distance downstream of the station where the secondary instabilities begin to amplify, and, hence, the growth-rate magnitudes are still moderate at this location. The peak-growth frequency is approximately 65 kHz for mode 1. Here, mode 1 is a z mode, mode 2 a y mode, mode 3 a z mode, and mode 4 a y mode. The corresponding eigenfunctions near their respective peaks are plotted in Fig. 20, with the faint white lines representing the underlying stationary crossflow vortex.

Similarly, the secondary-instability-mode growth rates for the control mode are plotted in Fig. 21 as a function of frequency at $X/C = 0.126$. The peak frequency is found to be approximately 90 kHz for mode 1, a y mode. The corresponding eigenfunctions are shown in Fig. 22.

IV. Conclusions

A computational analysis has been performed for a laminar-flow test article designed to demonstrate DRE technology at flight Reynolds numbers of relevance to transport aircraft. The Mach number and sweep angle used in the analysis are 0.75 and 34.6 deg, respectively. Computations are performed using NPSEs and secondary-instability analysis for chord Reynolds numbers of 17×10^6, 24×10^6, and 30×10^6.

Various simplifying assumptions have been made in this study for extending swept-wing NLF using the DREs. The infinite-swept

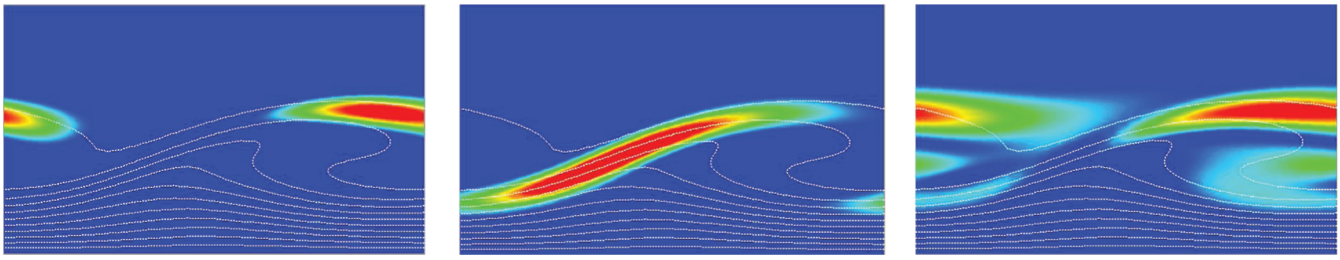

a) Mode1: a y-mode b) Mode 2: a z-mode c) Mode 3: a y-mode

Fig. 22 Chordwise-velocity eigenfunctions for the three modes corresponding to Fig. 21.

airfoil assumption does not adequately represent the flowfield on the glove, as the fully 3-D boundary layer on the glove is much less unstable than the infinite-swept case. In addition, the same C_p distribution is chosen for the three flight Reynolds numbers; therefore, the results reported and conclusions drawn are specific to the selected C_p distribution. The initial amplitudes of the target and control modes, and the associated mode shapes are arbitrarily chosen. For example, linear eigenmode was used to initialize the calculation, but it is not known how far downstream of the DRE such a mode shape develops and what is the relation of its amplitude to the height and shape of the roughness. Similarly, the initial target-mode amplitudes are related to the specific surface finish, but these amplitudes were assumed in this study. Because of these assumptions, conclusions drawn from the present results can be characterized as qualitative at best. Definitive conclusions can only be drawn when the initial modal amplitudes are available from a careful receptivity analysis for a given surface finish and DRE roughness height, shape, and location.

The computations performed in this study have demonstrated that crossflow-induced transition can be delayed if the control mode of a given wavelength and amplitude is introduced. One of the goals of the flight experiment was to demonstrate that DREs can delay transition by 50%, which does not seem to be fully supported by these computations. The present computations show that DREs could delay transition by about 20% for the pressure distribution and flight Reynolds numbers used in the study. These results are based on the secondary-instability analysis of the mean flow in the presence of stationary crossflow disturbances. Several high-frequency secondary-instability modes are present for the target- and control-mode wavelengths. The most unstable secondary-instability mode is a z mode for the target, but a y mode in case of the smaller-wavelength control mode.

Computations were also performed to study the effect of DRE on traveling crossflow disturbances. The wavelength of the most amplified traveling disturbance (the target mode) was 12 mm, and the stationary control mode had a wavelength of 4 mm. The same control mode was used to delay the growth of the stationary target mode of wavelength 8 mm. It is shown that DRE with the 4 mm wavelength suppresses the growth of the traveling mode of frequency 1 kHz as well.

In summary, the following conclusions can be drawn from this analysis:

1) DREs could delay crossflow-induced transition by about 20% at Reynolds number in the range of 17×10^6 to 30×10^6.

2) In addition to the stationary crossflow disturbances, DREs are found to suppress the growth of most amplified traveling disturbances.

Acknowledgment

This work was performed in support of NASA's Environmentally Responsible Aviation Project.

References

[1] Hefner, J. N., and Bushnell, D. M., "An Overview of Concepts for Aircraft Drag Reduction," *Special Course on Concepts for Drag Reduction*, AGARD Rept. No. 654, Essex, England, U.K., 1977, pp. 1–30.

[2] Marec, J.-P., "Drag Reduction: A Major Task for Research," *CEAS/DragNet European Drag Reduction Conference 2000*, Springer–Verlag, Berlin, June 2000, pp. 17–28.

[3] Drake, A., Harris, C. A., Komadina, S. C., Wang, D. P., and Bender, A. M., "Environmentally Responsible Aviation N+2 Advanced Vehicle Study," *Northrop Grumman Systems Corporation Final Technical Report*, NASA CR-2013-218304, 2013.

[4] Bushnell, D. M., and Tuttle, M. H., "Survey and Bibliography on Attainment of Laminar Flow Control in Air Using Pressure Gradient and Suction," Vol. 1, NASA RP-1035, 1979.

[5] Bushnell, D. M., "Overview of Aircraft Drag Reduction Technology," *Special Course on Skin Friction Drag Reduction*, AGARD Rept. 786, Essex, England, U.K., 1992.

[6] Joslin, R. D., "Aircraft Laminar Flow Control," *Annual Review of Fluid Mechanics*, Vol. 30, No. 1, 1998, pp. 1–29. doi:10.1146/annurev.fluid.30.1.1

[7] Green, J. E., "Laminar Flow Control—Back to the Future?" AIAA Paper 2008-3738, June 2008.

[8] Spalart, P. R., and McLean, J. D., "Drag Reduction: Enticing Turbulence, and Then an Industry," *Philosophical Transactions of the Royal Society of London, Series A: Mathematical and Physical Sciences*, Vol. 369, No. 1940, 2011, pp. 1556–1569. doi:10.1098/rsta.2010.0369

[9] Wilkinson, S. P., and Malik, M. R., "Stability Experiments in the Flow over a Rotating Disk," *AIAA Journal*, Vol. 23, No. 4, 1985, pp. 588–595. doi:10.2514/3.8955

[10] Dagenhart, J. R., Saric, W. S., Mousseux, M. C., and Stack, J. P., "Crossflow-Vortex Instability and Transition on a 45-Degree Swept Wing," AIAA Paper 1989-1892, June 1989.

[11] Balachandar, S., Streett, C. L., and Malik, M. R., "Secondary Instability in a Rotating Disk Flow," *Journal of Fluid Mechanics*, Vol. 242, No. 1, 1992, pp. 323–347. doi:10.1017/S0022112092002398

[12] Malik, M. R., Li, F., and Chang, C.-L., "Crossflow Disturbances in Three-Dimensional Boundary Layers: Nonlinear Development, Wave Interaction and Secondary Instability," *Journal of Fluid Mechanics*, Vol. 268, No. 1, 1994, pp. 1–36. doi:10.1017/S0022112094001242

[13] Malik, M. R., Li, F., Choudhari, M., and Chang, C.-L., "Secondary Instability of Crossflow Vortices and Swept-Wing Boundary-Layer Transition," *Journal of Fluid Mechanics*, Vol. 399, Nov. 1999, pp. 85–115. doi:10.1017/S0022112099006291

[14] Kohama, Y., Saric, W. S., and Hoos, J. A., "A High-Frequency Secondary Instability of Crossflow Vortices that Leads to Transition," *Boundary Layer Transition and Control: Proceedings of the Royal Aeronautical Society*, Cambridge, England, U.K., April 1991.

[15] White, E. B., and Saric, W. S., "Secondary Instability of Crossflow Vortices," *Journal of Fluid Mechanics*, Vol. 525, Feb. 2005, pp. 275–308. doi:10.1017/S002211200400268X

[16] Maddalon, D., Fisher, D., Jennett, L., and Fischer, M., "Simulated Airline Service Experience with Laminar Flow Control Leading-Edge System," *NASA Symposium on NLF and LFC Research*, NASA CP-24587, 1987, pp. 195–218.

[17] Collier, F., "An Overview of Recent Subsonic Laminar Flow Control Flight Experiments," AIAA Paper 1993-2987, July 1993.

[18] Pfenninger, W., "Laminar Flow Control Laminarization," *Special Course on Drag Reduction*, AGARD Rept. 654, Essex, England, U.K., 1977.

[19] Anders, S. G., and Fischer, M. C., "F-16XL-2 Supersonic Laminar Flow Control Flight Test Experiment," NASA TP-1999-209683, 1999.

[20] Saric, W. S., Carrillo, R. B. Jr., and Reibert, M. S., "Nonlinear Stability and Transition in 3-D Boundary Layers," *Meccanica*, Vol. 33, No. 5, 1998, pp. 469–487. doi:10.1023/A:1004368526215

[21] Chang, C.-L., and Choudhari, M., "Boundary-Layer Receptivity and Integrated Transition Prediction," AIAA Paper 2005-0526, Jan. 2005.

[22] Wassermann, P., and Kloker, M., "Mechanisms and Passive Control of Crossflow-Vortex-Induced Transition in a Three-Dimensional Boundary Layer," *Journal of Fluid Mechanics*, Vol. 456, April 2002, pp. 49–84. doi:10.1017/S0022112001007418

[23] Li, F., Choudhari, M. M., Chang, C.-L., Streett, C. L., and Carpenter, M. H., "Computational Modeling of Roughness-Based Laminar Flow Control on a Subsonic Swept Wing," *AIAA Journal*, Vol. 49, No. 3, March 2011, pp. 520–529. doi:10.2514/1.J050503

[24] Li, F., Choudhari, M. M., Carpenter, M. H., Malik, M. R., Chang, C.-L., and Streett, C. L., "Roughness Based Crossflow Transition Control for a Swept Airfoil Design Relevant to Subsonic Transports," AIAA Paper 2010-4380, July 2010.

[25] Saric, W. S., Carpenter, A. L., and Reed, H. L., "Passive Control of Transition in Three-Dimensional Boundary Layers, with Emphasis on Discrete Roughness Elements," *Philosophical Transactions of the Royal Society of London, Series A: Mathematical and Physical Sciences*, Vol. 369, No. 1940, 2011, pp. 1352–1364. doi:10.1098/rsta.2010.0368

[26] Belisle, M. J., Roberts, M. W., Tufts, M. W., Tucker, A. A., Williams, T., Saric, W. S., and Reed, H. L., "Design of the Subsonic Aircraft Roughness Glove Experiment (SARGE)," AIAA Paper 2011-3524, June 2011.

[27] Malik, M., Liao, W., Lee-Rausch, E., Li, F., Choudhari, M., and Chang, C.-L., "Computational Analysis of the G-III Laminar Flow Glove," AIAA Paper 2011-3525, June 2011.

[28] Hartshorn, F., Belisle, M. J., and Reed, H. L., "Computational Optimization of a Natural Laminar Flow Experimental Wing Glove," AIAA Paper 2012-0870, Jan. 2012.

[29] Liao, W., Malik, M. R., Lee-Rausch, E. M., Li, F., Nielsen, E. J., Buning, P. G., Chang, C. L., and Choudhari, M., "Boundary-Layer Stability Analysis of the Mean Flows Obtained Using Unstructured Grids," *Journal of Aircraft*, Vol. 52, No. 1, 2015, pp. 49–63. doi:10.2514/1.C032583

[30] Roberts, M. W., Reed, H. L., and Saric, W. S., "A Transonic Laminar-Flow Wing Glove Flight Experiment: Computational Evaluation and Linear Stability," AIAA Paper 2012-2668, June 2012.

[31] Nichols, R., and Buning, P., *User's Manual for OVERFLOW 2.1*, NASA Langley Research Center, Hampton, VA, 2010, http://people.nas.nasa.gov/~pulliam/Overflow/Overflow_Manuals.html [retrieved Feb. 2015].

[32] Wie, Y.-S., "BLSTA—A Boundary Layer Code for Stability Analysis," NASA CR-4481, 1992.

[33] Chang, C.-L., "The Langley Stability and Transition Analysis Code (LASTRAC): LST, Linear and Nonlinear PSE for 2-D, Axisymmetric, and Infinite Swept Wing Boundary Layers," AIAA Paper 2003-0974, Jan. 2003.

[34] Swearingen, J. D., and Blackwelder, R. F., "The Growth and Breakdown of Streamwise Vortices in the Presence of a Wall," *Journal of Fluid Mechanics*, Vol. 182, No. 1, 1987, pp. 255–290. doi:10.1017/S0022112087002337

[35] Li, F., and Malik, M. R., "Fundamental and Subharmonic Secondary Instability of Görtler Vortices," *Journal of Fluid Mechanics*, Vol. 297, No. 1, 1987, pp. 77–100. doi:10.1017/S0022112095003016

[36] Li, F., and Choudhari, M. M., "Spatially Developing Secondary Instabilities and Attachment Line Instability in Supersonic Boundary Layers," AIAA Paper 2008-0590, Jan. 2008.

[37] Li, F., and Choudhari, M. M., "Spatially Developing Secondary Instabilities in Compressible Swept Airfoil Boundary Layers," *Journal of Theoretical and Computational Fluid Dynamics*, Vol. 25, Nos. 1–4, June 2011, pp. 65–84. doi:10.1007/s00162-010-0190-x

[38] Deyhle, H., and Bippes, H., "Disturbance Growth in an Unstable Three-Dimensional Boundary Layer and Its Dependence on Environmental Conditions," *Journal of Fluid Mechanics*, Vol. 316, No. 1, 1996, pp. 73–113. doi:10.1017/S0022112096000456

[39] Radeztsky, R. H., Reibert, M. S., Saric, W. S., and Takagi, S., "Effect of Micron-Sized Roughness on Transition in Swept-Wing Flows," AIAA Paper 1993-0076, Jan. 1993.

[40] Crouch, J. D., and Ng, L. L., "Variable N-Factor Method for Transition Prediction in Three-Dimensional Boundary Layers," *AIAA Journal*, Vol. 38, No. 2, 2000, pp. 211–216. doi:10.2514/2.973

[41] Choudhari, M., Chang, C.-L., Streett, C. L., and Balakumar, P., "Integrated Transition Prediction: A Case Study in Supersonic Laminar Flow Control," AIAA Paper 2003-0973, Jan. 2003.

[42] Choudhari, M., Chang, C.-L., and Jiang, L., "Towards Transition Modeling for Supersonic Laminar Flow Control," *Philosophical Transactions of the Royal Society of London, Series A: Mathematical and Physical Sciences*, Vol. 363, No. 1830, 2005, pp. 1041–1259. doi:10.1098/rsta.2005.1551

[43] White, E. B., and Saric, W. S., "Secondary Instability of Crossflow Vortices," *Journal of Fluid Mechanics*, Vol. 525, Feb. 2005, pp. 275–308. doi:10.1017/S002211200400268X

D. Gaitonde
Associate Editor